Electrochemical and Solid-State Letters, **10** (7) A171-A175 (2007)
1099-0062/2007/10(7)/A171/5/$20.00 © The Electrochemical Society

Electrochemical Capacitor of $MnFe_2O_4$ with Organic Li-Ion Electrolyte

Shin-Liang Kuo and Nae-Lih Wu*,z

Department of Chemical Engineering, National Taiwan University, Taipei, Taiwan 106

$MnFe_2O_4$ nanocrystallites have been found to exhibit capacitive characteristics in organic electrolyte containing 1 M $LiPF_6$ in a mixture of ethyl carbonate + ethylene methyl carbonate up to 4.5 V vs Li/Li^+. The ferrite exhibits a capacitance of 126 F/g-$MnFe_2O_4$, and the symmetric-cell demonstrated a stable working voltage window of 2.5 V. In situ synchrotron spectroscopic analysis identified valence change at Mn-ion sites and a very small ($<1\%$) extent of lattice variation, in response to Li-ion insertion/extraction. Compared with other pseudocapacitive oxides with Li-ion electrolytes, the present ferrite system has demonstrated superior cycling stability under high-rate cycling.
© 2007 The Electrochemical Society. [DOI: 10.1149/1.2737541] All rights reserved.

Manuscript submitted December 26, 2006; revised manuscript received April 2, 2007. Available electronically May 10, 2007.

Compared with batteries, electrochemical capacitors have the potential for providing higher power density and good cyclability.[1-3] They are generally categorized into two types based on the charge-storage mechanism. The electric double-layer capacitance (EDLC) arises from electrostatic separation of charges at the interface between electrode and electrolyte. Pseudocapacitance results from either superficial or multielectron-transfer faradaic reactions with fast charge/discharge properties.

An increasing number of metal oxides exhibiting pseudocapacitive behaviors have been discovered in recent years, but they are mainly in aqueous electrolytes. They include amorphous-(a-)$MnO_2{\cdot}nH_2O$ [4-6] and $MnFe_2O_4$ [7] in aqueous alkali chloride solutions and Fe_3O_4 in aqueous sulfites solutions.[8,9] Although $MnFe_2O_4$ has a structure close to Fe_3O_4, its electrochemical behaviors in aqueous electrolytes resemble those of the a-MnO_2 electrochemical capacitor. Its redox mechanism has been identified[10] to involve charge transfer at both the Mn- and Fe-ion sites over respective potential ranges, balanced by insertion/extraction of proton into/from the lattice.

The energy density (E) of an electrochemical capacitor is equal to $1/2C\Delta V^2$, where C is capacitance and ΔV is the working voltage window. Therefore, the energy density of an electrochemical capacitor benefits greatly from the employment of organic electrolytes, which typically give two to three times wider working voltage windows than the aqueous ones. Progress in exploring organic-electrolyte electrochemical capacitors of metal oxides, nevertheless, has been less successful than in aqueous ones. Some recent studies along this line have focused on potential cathode oxide materials for Li-ion batteries, such as V_2O_5 [11-13] and MnO_2.[14] In spite of large initial capacitances, poor cycling stability (typically less than a couple hundred cycles) is the major concern for these materials. Furthermore, the reported electrochemical responses for either the vanadium or manganese oxides materials are, in fact, more of a battery (cathode) than of a capacitor.

An organic pseudocapacitive system, namely $MnFe_2O_4$ in organic Li-ion electrolyte, exhibiting capacitive behavior is reported here. Important electrochemical and solid-state chemical properties of the system were characterized by electrochemical and in situ synchrotron X-ray analyses. Most notably, this system has demonstrated superior stability under high-rate cycling, as compared with the other organic pseudocapacitive systems reported in the literature.

Experimental

$MnFe_2O_4$ nanocrystallites were synthesized to deposit onto conductive acetylene black (AB, Vulcan XC72, Cabot Corporation) as follows. $MnSO_4$ was dissolved along with $FeCl_3$ with a stoichiometric ratio of 1:2 in 1 M HCl aqueous solution with bubbling N_2, followed by adding the predetermined amount of AB powder. The solution was then added into the solution that contained 1.5 M NaOH under vigorous stirring. Black precipitate was immediately formed upon mixing. It was found that the AB particles sedimented simultaneously with the oxide precipitate, suggesting that the oxide component was homogeneously combined with the AB particles during the synthesis process. The supernatant liquid was then decanted and fresh deionized water was added. Repeated solution-decanting and water-replenishing processes were carried out to remove residual anions. Finally, the powder was dried in air at 50°C, followed by calcination at 350°C for 2 h in N_2. The final powders had a weight ratio of the oxide to AB $\sim$ 1:1.

Electrodes were made of the composite powder, polyvinylidene fluoride (PVdF) in 10 wt % and Al foil as current collector. After being dried at 150°C in a vacuum oven for 24 h, the electrode sheets were punched into 1.2 cm diameter disks for assembly into coin-cells. Analyses were conducted with either "half-cell" or "symmetric-cell" configuration. The half-cell configuration consisted of an oxide/AB working electrode and a Li-foil counter electrode, while the symmetric cell contained two oxide/AB electrodes. The electrolyte was 1 M $LiPF_6$ in a 50/50 (vol %) mixture of ethyl carbonate (EC) and ethylene methyl carbonate (EMC). All the cells were assembled in a dry room where the dew point was maintained at between -40 and -45°C. Cyclic voltammetry (CV) and chronopotential curves were recorded by an electrochemical analyzer (Eco Chemie PGSTAT30). The average specific capacitance of the electrodes was calculated from the CV curve as follows

$$C_{\text{avg}} = \Delta Q(w \times \Delta V)^{-1} = \left(\int I\mathrm{dV}\right)(s \times \Delta V \times w)^{-1} \qquad [1]$$

where ΔQ is the total amount of charge accumulated over a potential window ΔV, w is the mass of active material in one electrode, I is the current, and s is the potential scan rate.

Synchrotron X-ray diffraction (XRD) and X-ray absorption near-edge spectroscopy (XANES) were conducted, respectively, at beam lines 01C2 and 17C1 of the National Synchrotron Radiation Research Center (NSRRC) in Taiwan, and the half-cell configuration of the electrochemical cell was adopted in both analyses. For the in situ measurements, the covers on both sides of the coin cell were first perforated and then sealed with Kapton foils in order to allow the X-ray beam to pass through the cell. For the in situ XANES experiment, CV was run at a scan rate of 0.2 mV/s, and the scan was interrupted at each selected potential for 10 min for data collection. For the in situ XRD, CV was run at the same rate, and the patterns were recorded with a translating curved imaging plate (Fuji BAS2500) with a sample-to-film distance of 280 mm. Two-dimensional data were converted using the FIT2D program.

* Electrochemical Society Active Member.
z E-mail: nlw001@ntu.edu.tw

Downloaded 27 Nov 2008 to 140.112.113.225. Redistribution subject to ECS license or copyright; see http://www.ecsdl.org/terms_use.jsp

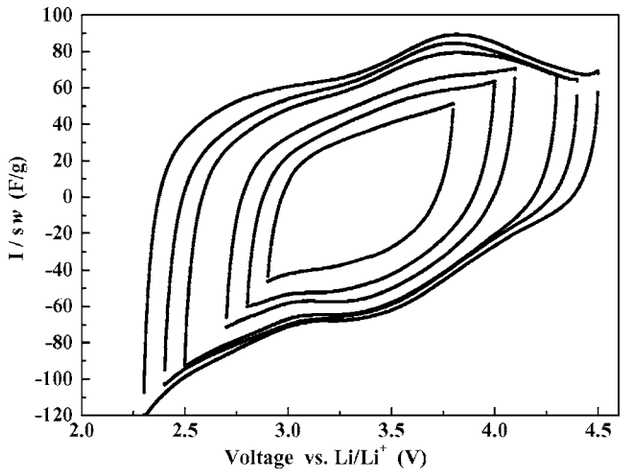

Figure 1. Cyclic voltammograms of half-cell consisting of $MnFe_2O_3$/AB (1:1 by weight) composite electrode against Li (electrolyte: 1 M $LiPF_6$ in EC + EMC; voltage scan rate: 2 mV/s).

Results and Discussion

The microstructures of the composite powders have been described in detail in our previous study of the aqueous system.[15] In brief, the ferrite phase is crystalline and has a face-centered cubic spinel structure with an average crystallite size of ~13 nm. It has been confirmed by transmission electron microscopy that the crystallites are randomly deposited on AB particles. N_2 adsorption measurements showed that the composite powder has a porous structure containing predominantly mesopores with a total surface area of ~160 m^2/g. Most of the surface area comes from AB, which has an original surface area of 220 m^2/g.

Figure 1 shows the voltammograms obtained from the half-cell configuration, where the counter electrode is a Li foil. Two characteristics were noticed. First, the current profiles are close to rectangular shape, characteristic of a capacitor, except with broad redox humps within the middle portion of the voltage range. The profile is completely different from those of the previously reported oxides, including V_2O_5 and MnO_2,[11-14] which show peaks of redox reaction pairs. Second, the response current, and hence the capacitance of the electrode, was found to increase with increasing swept voltage range.

The inclination of the voltammograms in Fig. 1 may easily be mistaken as an indication of high equivalent serial resistance (ESR), but careful examination of other features of the curve profiles suggests the otherwise. In particular, it is noted that for all the voltammograms, the transition in response-current upon potential-scan reversal is very fast at both ends of the potential windows, suggesting actually a small ESR. This is further supported by the symmetric-cell data shown below. Accordingly, the inclination of the voltammogram mainly indicates the strong potential-dependent nature of the capacitance of the oxide.

Calculation according to Eq. 1 using the data between 2.5 and 4.5 V shown in Fig. 1 gives an average specific capacitance of 69 F/g for the composite powder. The contribution from the AB component is estimated from the data of pure AB electrode, which gives ~12.0 F/g-C. Accordingly, the specific capacitance for the ferrite component is 126 F/g-$MnFe_2O_4$ between 2.5 and 4.5 V. For comparison, the specific capacitance of the ferrite phase in aqueous electrolytes is ~105 F/g-$MnFe_2O_4$ [15] and the working voltage window is 1.0 V. There is a fivefold increase in energy density due to the replacement of aqueous electrolyte with the organic Li-ion electrolyte. Finally, the upper voltage limit is about 4.5 V (vs the Li/Li^+ electrode), beyond which strong redox peaks start to evolve gradually in the voltammograms. That is, the cell transforms from capacitor-like to battery-like. This transformation is irreversible, and once it occurs, the capacitance fades rapidly upon cycling.

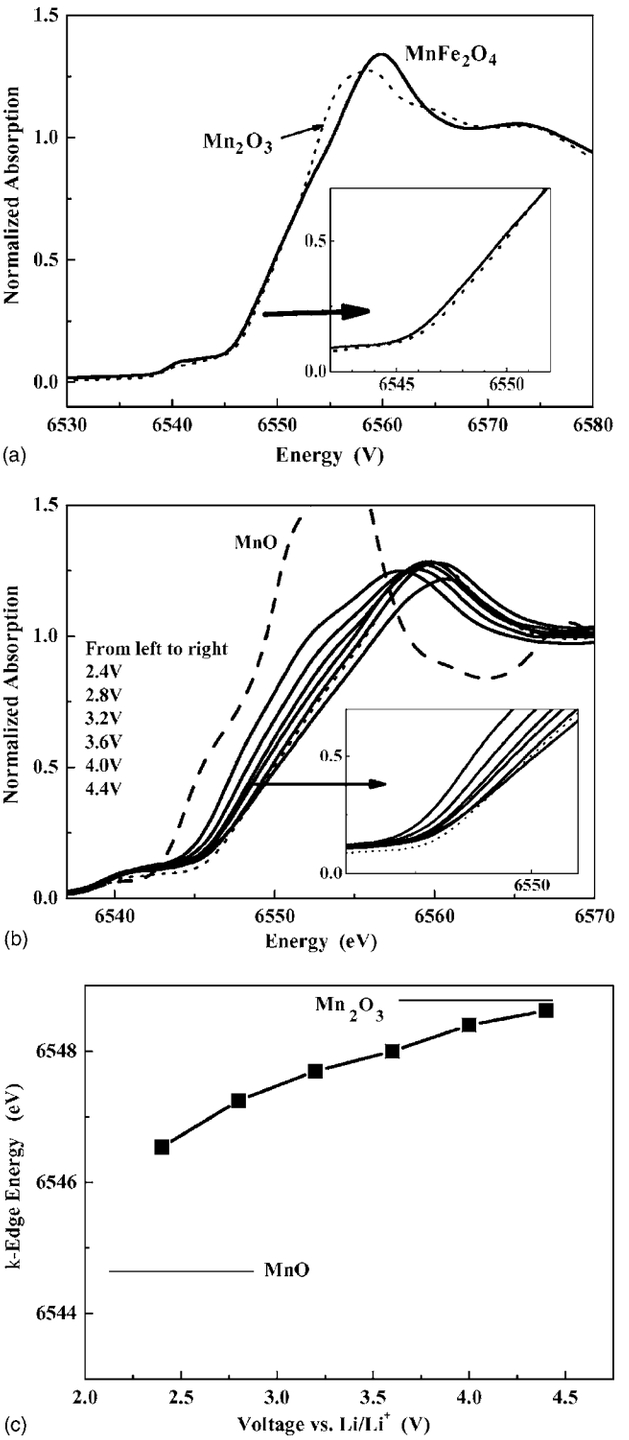

Figure 2. XANES data: (a) curves acquired from as-synthesized $MnFe_2O_4$ and Mn_2O_3 standard and (b) curves acquired in situ during the discharge (lithiation) phase at indicated voltages. The dotted curve denotes the as-synthesized state, while the dashed curve indicates the MnO standard. (c) The *k*-edge absorption energy determined from b.

In situ XANES spectra of Mn K-edge of the as-synthesized composite powder were shown in Fig. 2a. Spectrum of Mn_2O_3 is also shown for comparison. Each XANES spectrum can be divided into

Downloaded 27 Nov 2008 to 140.112.113.225. Redistribution subject to ECS license or copyright; see http://www.ecsdl.org/terms_use.jsp

a pre-edge region A (~6537–6545 eV) containing weak peaks, a main edge region B (6545–6555 eV), and resonance peak regions C (6555–6566 eV) and D (6566–6580 eV).[16-18] The peaks within pre-edge region A are ascribed to 1s → 3d transitions.[16] The main absorption region B can be assigned[16,18] to the transition from 1*s* to *p*-like states of t_{1u} symmetry. The edge energy is conventionally taken as the energy at the first inflection point, and it is known to increase with increasing valence of the transition-metal ion within the oxides.[16-18] It was found that the Mn ions in the as-synthesized state have a valence close to three, as the edge energy matches closely with that of Mn_2O_3. It has previously been shown[10] by the extended X-ray absorption fine structure (EXAFS) analysis that the Mn ions are randomly distributed over the tetrahedral and octahedral metal-ion sites within the spinel structure.

Figure 2b showed the XANES spectra measured in situ during CV cycling. The spectrum of MnO is also shown for comparison. First, it was found that at open-circuit voltage (OCV, ~3.3 V) the edge energy is actually lower than that of the as-synthesized powder shown in Fig. 2a. Second, upon CV cycling, the edge front was found to shift toward lower energies during the negative scan, while it moves back to pass over the OCV position and to higher energies during the positive scan. The edge energy data of Mn ions are plotted as a function of voltage in Fig. 2c, and they were shown to fall between those of Mn^{+3} and Mn^{+2}. The results give direct evidence to the notion that charge-transfer takes place at the Mn-ion sites, balanced by Li insertion/extraction. In addition, the data may also indicate that the upper critical voltage limit (~4.5 V) to the battery-like transformation corresponds to when the valence of Mn ions is about to exceed +3.

The XANES spectra of Fe were interfered by the signals from the stainless-steel case of the coin cell. As a result, the variation in valence of the Fe ion during the CV cycling cannot be verified. However, in the case of aqueous electrolytes,[10] charge-transfer at the Fe-ion sites was identified to take place within the potential window between 0.1 and 0.5 vs Ag/AgCl/saturated KCl [EG&G, 197 mV vs normal hydrogen electrode (NHE) at 25°C], giving rise to redox humps in the CV plot. That potential window, equivalent to 3.34–3.74 V vs Li/Li^+, overlapped partially with the voltage range where redox humps were observed in the present study (Fig. 1). It, thus, does not rule out the possibility that charge-transfer at the Fe-ion sites may also take place in the present organic electrolyte.

The decrease in Mn *k*-edge binding energy at the OCV state as compared with the as-synthesized state (Fig. 2a and b) may indicate that part of the Mn ions are reduced when the cell has been assembled. A similar phenomenon has also been observed in the aqueous system, which involves insertion/extraction of protons.[10] In the present system, the reduction process apparently takes place in conjunction with insertion of Li ions into the oxide lattice. This, as shown later, enables the operation of the symmetric configuration, where no Li electrode is involved. The nature of the oxidation counterpart has yet to be identified. It might involve oxidation of solvent species.

For in situ synchrotron XRD patterns, no new peak was observed, suggesting that no phase change occurs during the CV cycling. Rather, the peaks of the ferrite phase were clearly seen to shift back and forth upon cycling. For instance, as shown in Fig. 3, the (311) peak, which has the strongest intensity, of the ferrite phase was shown to shift toward lower angles, suggesting lattice expansion, during the negative scan (i.e., Li insertion) and then back to the original positions during the positive scan (Li extraction). The structural variation is reversible. The extent of lattice expansion of this reflection between 4.4 and 2.4 V is merely 0.68%.

The cyclic voltammograms of symmetric cell over different working voltage range are shown in Fig. 4a. The capacitance of the cell was also found to increase with increasing scanned voltage range, consistent with the half-cell behavior. A stable working voltage window of 2.5 V without the irreversible transformation to the battery-like behavior was determined. Figure 4b shows the voltammograms at different scan rates up to 100 mV/s. Capacitance drops most significantly when the scan rate varies from 4 to 20 mV/s and then levels off at higher rates. The cell retains ~60% of the capacitance, which gives approximately ~75 F/g-$MnFe_2O_4$, as the scan rate increases from 2 to 100 mV/s.

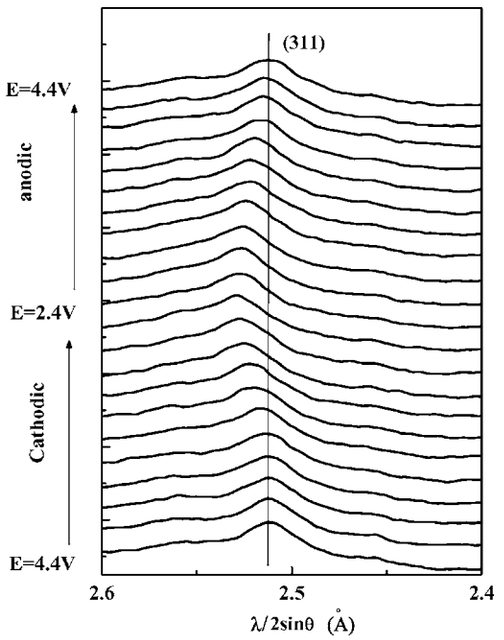

Figure 3. In situ synchrotron XRD patterns acquired during the course of charging/discharging cycle. The diffraction peak is the (311) reflection of $MnFe_2O_4$.

Some of the voltammograms of the symmetric cell, particularly those at slow scan rates, appear inclined. Notably, the profiles become less inclined with increasing scan rate. This is completely opposite to the situations of high ESR, where the voltammogram is expected to become increasingly inclined, approaching a shuttle-shaped profile, with increasing scan rate. In fact, the observed profile inclination in Fig. 4b is a natural consequence of the fact that, as shown in Fig. 1, the cathodic branch of the single-electrode voltammogram is more potential-dependent (i.e., more inclined) than the anodic branch.

Figure 5 shows the chronopotential curves of a symmetric cell at different current densities. The nearly linear potential-vs-time relation once again indicates capacitor-like behavior. In all cases, the cell shows coulometric efficiency greater than 95%. In the earlier literature concerning the electrochemical properties of V_2O_5 and MnO_2,[11-14] only data of half-cell configuration were presented. One main difference between the half-cell and symmetric-cell configurations is that the former has a Li foil as an unlimited source of Li ion, and Li ions can continuously be inserted into the oxide down to a rather low potential. As a result, the reported data in the literature were almost exclusively within the voltage range below their OCVs,[11-14] reflecting the Li-insertion behavior of an anode material. The behavior of a symmetric cell depends additionally on the Li-extraction behavior taking place at potential (voltage) above OCV on the cathode side. Thus, the working voltage window of a symmetric cell may not be the same as that shown by a single electrode in the half-cell configuration. Unfortunately, this fact was mostly overlooked in the previous reports. In the present case, the working voltage range of the symmetric cell (~2.5 V) was found to be approximately two times that between OCV (~3.3 V vs Li/Li^+) and the upper critical voltage before the battery-like transformation (~4.5 V vs Li/Li^+) (Fig. 1). The symmetry to OCV indicates good reversibility between the Li-insertion and -extraction processes. In

Downloaded 27 Nov 2008 to 140.112.113.225. Redistribution subject to ECS license or copyright; see http://www.ecsdl.org/terms_use.jsp

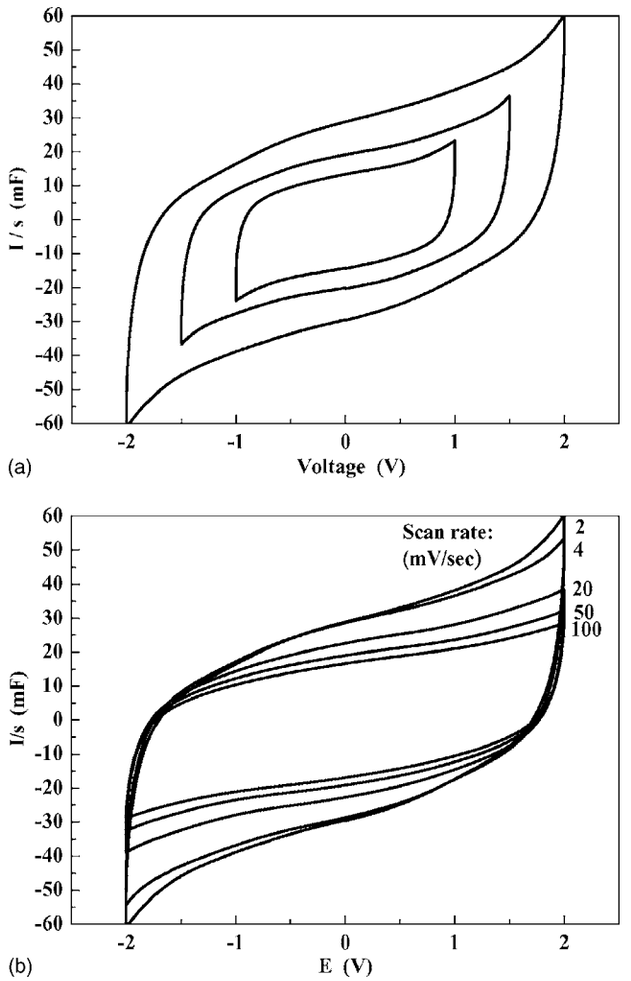

Figure 4. Cyclic voltammograms of symmetric cell, consisting of the two $MnFe_2O_4$/AB composite electrodes: (a) over different working voltage windows at the scan rate of 2 mV/s and (b) at different voltage scan rates.

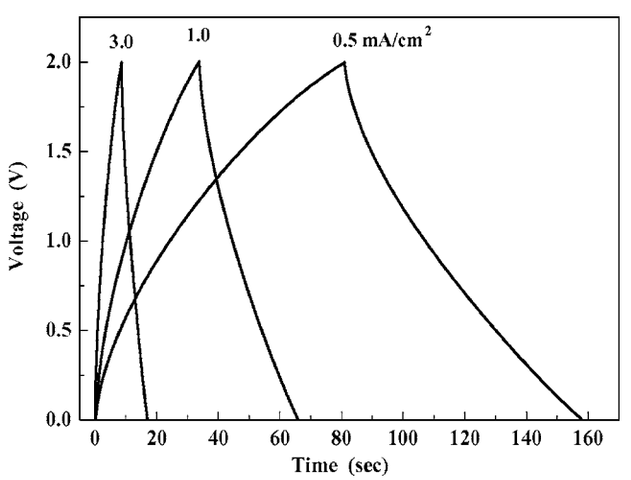

Figure 5. Chronopotential curves of symmetric $MnFe_2O_4$/AB (1:1 by weight) cell at different current densities (electrolyte: 1 M $LiPF_6$ in EC + EMC).

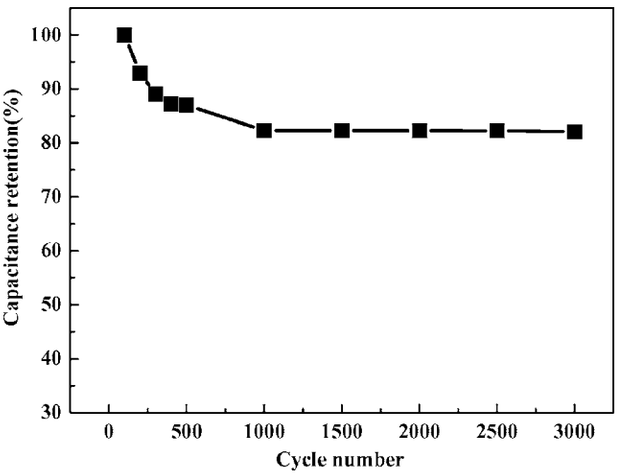

Figure 6. Capacitance retention vs cycle number for a symmetric cell (electrolyte: 1 M $LiPF_6$ in EC + EMC; current density: 3 mA/cm^2).

addition, the data suggest that the working voltage window of the symmetric cell is limited mainly by the stability limit on the cathode side. When the voltage of the symmetric cell exceeds 2.5 V, i.e., when the voltage of the cathode exceeds ~4.5 vs $LiLi^+$, accelerated fading sets in.

Compared with V_2O_5 and MnO_2 as potential pseudocapacitive electrode materials, the present ferrite electrode has a lower initial capacitance. However, superior cyclability may be its advantage. For instance, Mansour et al.[13] reported an initial discharge capacity of ~500 mAh/g, equivalent to a specific capacitance of 700 F/g, for an ambigel V_2O_5, but the ambigel showed ~70% loss after only 40 cycles at C/5 rate with no sign of leveling off. Watanabe et al.[14] reported the electrochemical properties of nanocrystalline Zn-doped MnO_2 materials. The oxides showed an maximum initial discharge capacity as high as ~200 mAh/g (or ~300 F/g), but most of them exhibited >30% capacity loss within 25 cycles even at 1 mV/s for CV. Figure 6 shows the capacitance retention of the present ferrite electrochemical capacitor cycled at the current density of 3 mA/cm^2, corresponding approximately to 50 mV/s (or 4.0 A/g-$MnFe_2O_4$). The capacitance decreased by ~18% during the first 1000 cycles and then remained unchanged throughout 3000 cycles. The present ferrite cell has demonstrated much improved cycling stability. The good cycling stability may have to do with the very small volume variation, as indicated by the in situ XRD data (Fig. 3), involved in the charge/discharge process.

Further research is ongoing to investigate the mechanisms behind some of the phenomena described above. For one, the dependence of capacitance on the scanned potential range is unique to the present ferrite cell and has not been reported for other pseudocapacitive oxides. For another, the oxidation reaction in conjunction with initial lithiation of the ferrite has yet to be identified. Finally, optimization in electrode structure for greater cycling stability will be indispensable for realizing its commercial potential.

Conclusion

$MnFe_2O_4$ has been found to exhibit capacitive characteristics in organic electrolyte of $LiPF_6$ in an EC + EMC mixture with a working voltage window up to 4.5 V vs Li/Li^+. The ferrite material has exhibited a specific capacitance of 126 F/g, and the symmetric-cell configuration has shown a stable working voltage window of 2.5 V. In situ XANES analysis identified valence change at the Mn-ion sites, while in situ XRD analysis detected lattice expansion/contraction of less than 1%. The ferrite electrode shows good cycling stability.

Downloaded 27 Nov 2008 to 140.112.113.225. Redistribution subject to ECS license or copyright; see http://www.ecsdl.org/terms_use.jsp

Acknowledgment

This work is supported by the National Science Council of Republic of China under contract no. NSC 95-2221-E-002-350-MY3 and by National Taiwan University under project no. 95R0066-BE04-01.

National Taiwan University assisted in meeting the publication costs of this article.

References

1. B. E. Conway, *J. Electrochem. Soc.*, **138**, 1539 (1991).
2. B. E. Conway, V. Briss, and J. Wojtowicz, *J. Power Sources*, **66**, 1 (1997).
3. R. Kötz and M. Carlen, *Electrochim. Acta*, **45**, 2483 (2000).
4. H. Y. Lee and J. B. Goodenough, *J. Solid State Chem.*, **144**, 220 (1999).
5. H. Y. Lee, V. Manivannan, and J. B. Goodenough, *C. R. Acad. Sci., Ser. IIc: Chim*, t. **2**, 565 (1999).
6. C. C. Hu and T. W. Tsou, *Electrochem. Commun.*, **4**, 105 (2002).
7. S. L. Kuo and N. L. Wu, *Electrochem. Solid-State Lett.*, **8**, A495 (2005).
8. N. L. Wu, S. Y. Wang, C. Y. Han, D. S. Wu, and L. R. Shiue, *J. Power Sources*, **113**, 173 (2003).
9. S. Y. Wang, K. C. Ho, S. L. Kuo, and N. L. Wu, *J. Electrochem. Soc.*, **153**, A75 (2006).
10. S. L. Kuo, J. F. Lee, and N. L. Wu, *J. Electrochem. Soc.*, **154**, A34 (2007).
11. H. H. Kim, J. H. Kim, B. W. Cho, Y. H. Lee, and K. B. Kim, *J. Electrochem. Soc.*, **153**, A989 (2006).
12. P. Gomez-Romero, M. Chojak, K. Cuentas-Gallegos, J. A. Asensio, P. J. Kulesza, N. Casan-Pastor, and M. Lira-Cantu, *Electrochem. Commun.*, **5**, 149 (2003).
13. A. N. Mansour, P. H. Smith, M. Balasubramanian, and J. McBreen, *J. Electrochem. Soc.*, **152**, A1312 (2005).
14. T. Watanabe, H. Zhou, and I. Honma, *J. Electrochem. Soc.*, **152**, A1568 (2005).
15. S. L. Kuo and N. L. Wu, *J. Power Sources*, **162**, 1437 (2006).
16. M. Belli, A. Scafati, A. Bianconi, S. Mobilio, L. Palladino, A. Reate, and E. Burattini, *Solid State Commun.*, **35**, 355 (1980).
17. B. Ammundsen, D. J. Jones, and J. Roziere, *J. Solid State Chem.*, **141**, 294 (1998).
18. N. Y. Safontseva and I. Y. Nikiforov, *Phys. Solid State*, **43**, 61 (2001).

Downloaded 27 Nov 2008 to 140.112.113.225. Redistribution subject to ECS license or copyright; see http://www.ecsdl.org/terms_use.jsp